

DAMAGE EVOLUTION AND FRICTIONAL HEATING IN A PBX  
MICROSTRUCTURE

A Thesis

Submitted to the Faculty

of

Purdue University

by

Rohan K. Tibrewala

In Partial Fulfillment of the

Requirements for the Degree

of

Master of Science in Mechanical Engineering

August 2019

Purdue University

West Lafayette, Indiana

**THE PURDUE UNIVERSITY GRADUATE SCHOOL**  
**STATEMENT OF THESIS APPROVAL**

Dr. Marisol Koslowski, Chair

School of Mechanical Engineering

Dr. Steven F. Son

School of Mechanical Engineering

Dr. Weinong Chen

School of Aeronautics and Astronautics

**Approved by:**

Dr. Jay P. Gore

Head of Departmental Graduate Program

To my parents and sister who have always encouraged and supported me in my endeavors.

## ACKNOWLEDGMENTS

I would like to thank my advisor Dr. Marisol Koslowski for giving me the opportunity to work on this project. Her supervision, guidance and continuous encouragement have been pivotal to the fulfillment of my masters thesis. I would like to thank Dr. Steven Son and Dr. Weinong Chen for participating in my thesis committee. I am also thankful to my teammates Dr. Nicolo Grilli, Dr. Yifei Zeng and Akshay Dandekar for their help and advice.

I would also like to thank my friends and family who have always supported me and helped me accomplish this work.

## TABLE OF CONTENTS

	Page
LIST OF TABLES . . . . .	vii
LIST OF FIGURES . . . . .	viii
SYMBOLS . . . . .	x
ABBREVIATIONS . . . . .	xi
ABSTRACT . . . . .	xii
1 INTRODUCTION . . . . .	1
1.1 Thesis Layout . . . . .	2
2 METHOD . . . . .	3
2.1 Phase Field Damage Model . . . . .	3
2.1.1 Griffith's Theory of Brittle Fracture . . . . .	3
2.1.2 Crack Topology Description . . . . .	5
2.1.3 Strain Energy . . . . .	6
2.2 Frictional Heat Source . . . . .	9
2.2.1 Numerical Model . . . . .	9
3 MODEL VALIDATION AND ANALYSIS . . . . .	11
3.1 Introduction . . . . .	11
3.2 Simulation Setup . . . . .	11
3.2.1 Mesh Sensitivity Analysis . . . . .	13
3.2.2 Length Scale Parameter Analysis . . . . .	15
3.2.3 $\eta$ Parameter Analysis . . . . .	16
3.2.4 Results for Multiple Loading Conditions . . . . .	17
3.3 Summary . . . . .	19
4 THERMAL-MECHANICAL ANALYSIS OF PBX MICROSTRUCTURES . . . . .	22
4.1 Simulation Setup . . . . .	22

	Page
4.2 Damage Evolution . . . . .	26
4.3 Temperature Evolution . . . . .	29
4.4 Cluster Analysis for Hotspot Intiation . . . . .	31
4.5 Dirty Binder . . . . .	33
4.6 Summary . . . . .	36
REFERENCES . . . . .	37
A STEPS INVOLVED IN INITIALIZATION OF THE PHASE FIELD DAM- AGE MODEL . . . . .	40

## LIST OF TABLES

Table	Page
3.1 Material properties used in the simulations [17–19]. . . . .	12
3.2 General mesh parameters employed in the simulations. . . . .	13
4.1 Material properties used in the simulations [27–31]. . . . .	24
4.2 Mesh parameters employed in the simulations. . . . .	24
4.3 Material properties used in the simulations. . . . .	34

## LIST OF FIGURES

Figure	Page
2.1 (a) Represents a domain $\Omega$ with a sharp internal discontinuity $\Gamma$ . (b) Represents the same domain but with the sharp discontinuity described using phase field. . . . .	4
2.2 1-D spatial representation of the crack surface. (a) Sharp crack at $x=0$ . (b) Diffuse crack at $x = 0$ modeled with length scale $l$ . . . . .	5
3.1 Domain employed in the Mode-1 displacement control simulations. . . . .	12
3.2 Phase field damage field for the same domain with varying element size. . .	14
3.3 Evolution of the crack tip velocity for three different mesh sizes. . . . .	14
3.4 Phase field damage field for three varying length scale paramaters. . . . .	15
3.5 Evolution of the crack tip velocity for three varying length scale parameters.	16
3.6 Evolution of the crack tip velocity for three varying length scale parameters.	17
3.7 Evolution of the crack tip for four varying displacement conditions. The mesh parameters used are $h = 160\mu m$ , $l_o = 5h$ and $\eta = 10ns/\mu m$ . . . . .	18
3.8 Evolution of the crack tip velocity for four varying displacement loading conditions. . . . .	19
3.9 The plot of crack velocities for different samples obtained from Zhou <i>et al.</i> [7].	20
4.1 The micro-structure [26] and the adopted area for mesh generation. . . . .	23
4.2 The domain generated after digitization depicting the type of boundary and loading conditions used. . . . .	24
4.3 The varying crack distributions used. (a) Crack Distribution-1 (b) Crack Distribution-2 (c) Crack Distribution-3 (d) Crack Distribution-4 (e) Crack Distribution-5. Initial crack density $\rho = 5\%$ ; Mean crack length= $12.5\mu m$ and a Standard Deviation in the crack length = $5\mu m$ . . . . .	25
4.4 Damage field and von Mises stress field plots for distribution-1. (a) $G_c = 2J/m^2$ ; $v = 100m/s$ (b) $G_c = 0.12J/m^2$ ; $v = 100m/s$ . Please note that the nodes with $c > 0.9$ have been removed for the Von-mises stress plots. .	27
4.5 Damage field plots of distribution-1 for loading velocity comparison.(a) $G_c = 0.12J/m^2$ ; $v = 50m/s$ (b) $G_c = 0.12J/m^2$ ; $v = 100m/s$ . . . . .	28

Figure	Page
4.6 Temperature field for distribution1.(a) $t = 100ns$ ; $v = 50m/s$ (b) $t = 100ns$ ; $v = 100m/s$ . The arrows indicate the hotspot with the maximum temperature. Please note that nodes with $c > 0.9$ have been removed. . . .	29
4.7 Temperature-time evolution plots for the hotspot with the maximum temperature. . . . .	30
4.8 Temperature-time evolution plots for the hotspot with the maximum temperature. . . . .	31
4.9 (a) $G_c = 2J/m^2$ ; $v = 50m/s$ (b) $G_c = 0.12J/m^2$ ; $v = 50m/s$ (c) $G_c = 2J/m^2$ ; $v = 100m/s$ (d) $G_c = 0.12J/m^2$ ; $v = 100m/s$ (e) $G_c = 0.12J/m^2$ ; $v = 10m/s$ . Hotspot temperature and size for various impact velocities and critical energy release rates. . . . .	32

## SYMBOLS

$m$	mass
$v$	velocity
$c$	phase field damage variable
$u$	displacement
$\epsilon$	strain
$\lambda, \mu$	Lamé constants
$\sigma$	stress
$\rho$	density
$G_c$	energy release rate
$C_r$	Rayleigh wave speed
$E$	Young modulus
$\nu$	poisson's ratio
$k$	thermal conductivity
$c_p$	Specific heat capacity

## ABBREVIATIONS

PBX	Polymer bonded explosive
HMX	High melting explosive
PMMA	Poly methyl methacrylate

## ABSTRACT

Tibrewala, Rohan K. M.Sc., Purdue University, August 2019. Damage Evolution and Frictional Heating in a PBX Microstructure. Major Professor: Marisol Koslowski, School of Mechanical Engineering.

In this study, dynamic crack propagation in brittle materials has been studied using a regularized phase field approach. The phase field model used has been validated using specific experimental results of a dynamic in-plane fracture. The crack branching phenomena and existence of a limiting crack tip velocity has been validated using a mode I simulation set-up. A parametric study has also been performed so as to normalize the various numerical parameters that affect the velocity at the crack tip. Following the validation of the phase field model a stochastic analysis of a PBX microstructure has been performed. The microstructure has a high HMX volume fraction of 79%. The energetic material is HMX and the binder used is Sylgard. Artificial defects are introduced in the system using phase field cracks. The analysis uses a finite element framework that accounts for various thermal-mechanical processes like deformation, heat generation, conduction, fracture and frictional heating at the crack surfaces. The effect on the temperature and damage field due to varying parameters like loading velocities and critical energy release rates is studied. Critical hotspot formation due to localized frictional heating is also studied. A concept of dirty binder is introduced to increase the grain volume fraction of the energetic in the composite. This amounts to a homogenized binder that accounts for the influence of the subsume particles that do not contribute to fracture but affect material properties of the binder.

## 1. INTRODUCTION

Polymer bonded explosives are materials that include explosive particles bounded in a polymer matrix. These materials typically contain 2-10% of polymer by mass and rest is comprised of the explosive material [1]. The properties of the PBX can be tailored to the specific needs depending on the type of polymer employed. Elastomers are employed with highly sensitive materials as it assuages the sensitivity of the particles towards mechanical stimuli like shock and friction. Fluoro-polymers are employed when the explosive material used is typically insensitive to mechanical stimuli. Energetic polymers are sometimes also used as a binder when the explosive power of the material needs to be increased. There are many such PBX that have been synthesized including PBX-9501, EDC-37, PBX-9502 etc. These include crystals like HMX, RDX, TATB, PETN etc. embedded in a matrix of binders like estane, sylgaard, polystyrene, polyurethane etc. These PBX are widely employed as propellants and ammunition. A great concern to explosive materials is the possibility of accidental ignition during manufacture and transport. Hence the study of the strength and failure properties of PBX is of great interest.

High energy density particles packed PBX is highly sensitive to mechanical and thermal stimuli. Growing pristine crystals having no defects is an extremely complicated and expensive process. Majority of the PBX manufactured contain pre-existing defects in the form of cracks and voids. The study of defects in PBX is important as it significantly affects the thermo-mechanical response of the material. Experiments indicate that damaged materials have higher sensitivity as compared to materials in pristine condition [2, 3]. The interaction of the stress wave with these microstructural defects leads to localized high temperature regions denoted as "hot-spots". These hot-spots are directly linked to the ignition threshold of the material. Hence it is very important to study the underlying mechanisms that lead to the hot-spot

formation. Some of the major mechanisms reported in various studies include void collapse, friction between crack surfaces, heat generation due to crack propagation etc [4–6]. Under mechanical stimulus these cracks tend to widen, propagate, branch etc leading to final failure. Understanding the underlying mechanisms behind the dynamic response of these materials is a great challenge.

## 1.1 Thesis Layout

The thesis is divided into four chapters. Chapter 2 describes the mathematical model employed for the computational analysis. First the phase field damage model is explained along with variations in the very same that alter its behaviour. In the latter part the frictional heating and its implementation is explained.

In Chapter 3, simulations are carried out on PMMA to study crack propagation, its limiting velocity and the crack branching phenomena. The results are validated using the experimental data obtained from Zhou *et al.* [7].

In Chapter 4 , a stochastic analysis of a PBX microstructure is performed to study the effect of artificial defects that are introduced in the system. Also hot-spot formation due to localized frictional heating is studied.

## 2. METHOD

### 2.1 Phase Field Damage Model

The easiest way to describe the phase field model is incorporation of a continuous field variable which enables a smooth transition between various physical phases within a given system. In the context of Fracture Mechanics, this variable is used to approximate a sharp crack discontinuity. The variable transitions smoothly from an intact phase to a completely damaged phase. The model employs the use of Griffith's theory of brittle fracture in combination with the conservation laws. The model was first proposed by Francfort and Marigo [8] to overcome the shortcomings of the classic failure mechanisms of Griffith [9] and Irwin [10]. Since then multiple improvements have been made to these models. Some of these model have been adopted into this research and will be explained in detail in the next section.

#### 2.1.1 Griffith's Theory of Brittle Fracture

We take an arbitrary domain  $\Omega \subset R^d$  (with  $d \in 1, 2, 3$ ). The body has an internal discontinuity  $\Gamma$  with an external boundary  $d\Omega$ . The displacement is given as  $\mathbf{u}(\mathbf{x}, t) \in R^d$ , where  $\mathbf{x}$  is a point on the domain and time  $t \in [0, T]$ . Assuming infinitesimal strain and linear isotropic elasticity, we define the strain tensor as

$$\epsilon_{ij} = u_{i,j} = \frac{1}{2} \left( \frac{\partial u_i}{\partial x_j} + \frac{\partial u_j}{\partial x_i} \right) \quad (2.1)$$

where  $i, j, k = 1, 2, 3$ . The elastic energy density is given by

$$a_e(\epsilon) = \frac{1}{2} \lambda \epsilon_{ii} \epsilon_{jj} + \mu \epsilon_{ij} \epsilon_{ij} \quad (2.2)$$

where  $\lambda$  and  $\mu$  are the Lamé constants. The energy equation has been described using two primary terms, kinetic energy and potential energy. The potential energy

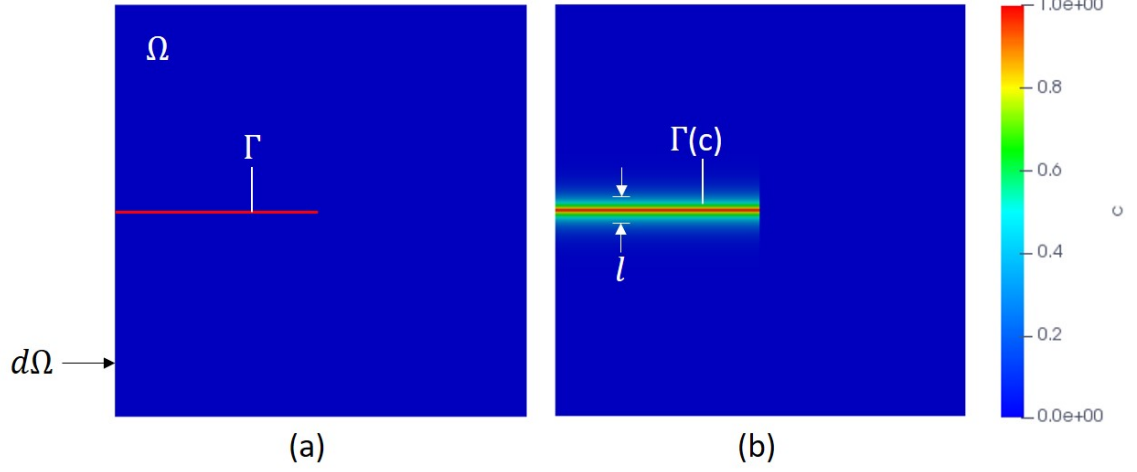


Fig. 2.1. (a) Represents a domain  $\Omega$  with a sharp internal discontinuity  $\Gamma$ . (b) Represents the same domain but with the sharp discontinuity described using phase field.

consists of the elastic energy and the fracture energy. According to Griffith's theory of brittle fracture the energy required to create a new fracture surface is equal to the surface energy. For brittle materials this surface energy is equivalent to the critical energy release rate  $G_c$ .

$$a_{pot}(\epsilon, \Gamma) = \int_{\Omega} a_e dx + \int_{\Gamma} G_c dx \quad (2.3)$$

Here the  $\Gamma$  term represents the crack surface density. The kinetic energy of the body is represented as

$$a_{kin}(\dot{u}) = \frac{1}{2} \int_{\Omega} \rho \dot{u}_i \dot{u}_i dx \quad (2.4)$$

Here  $\dot{u}$  is the partial derivative of the displacement field with respect to time as  $\dot{u} = \frac{\partial u}{\partial t}$  and  $\rho$  is the density of the material. Using the above equation we obtain the Lagrangian of the given problem as:

$$L(\epsilon, \dot{u}, \Gamma) = a_{kin}(\dot{u}) - a_{pot}(\epsilon, \Gamma) - \int_{\Omega} \left[ \frac{1}{2} \rho \dot{u}_i \dot{u}_i - a_e \right] dx - \int_{\Gamma} G_c dx \quad (2.5)$$

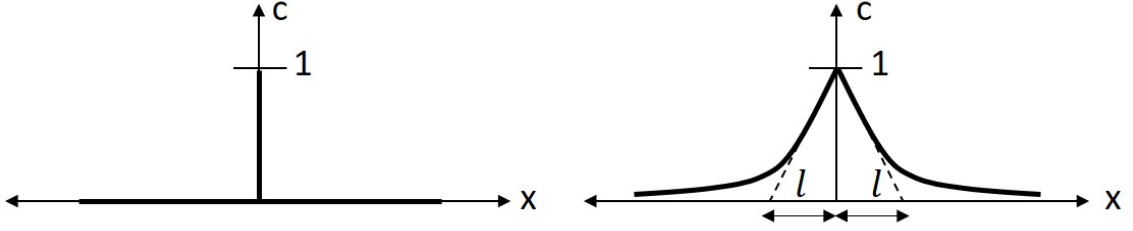


Fig. 2.2. 1-D spatial representation of the crack surface. (a) Sharp crack at  $x=0$ . (b) Diffuse crack at  $x = 0$  modeled with length scale  $l$ .

### 2.1.2 Crack Topology Description

A diffusive crack topology is preferred to smear the sharp topology of the crack surface. This sharp crack topology is described by using a field variable  $c(x) \in [0, 1]$ .  $c = 0$  represents an undamaged pristine material while  $c = 1$  represents a fully damaged material. Thus relating to the continuum theory  $c(x)$  represents a damage phase field which in turn represents discontinuities like microscopic cracks and voids. The phase field is approximated by the exponential function given as:

$$c(x) = e^{-\frac{|x|}{l}} \quad (2.6)$$

Here  $l$  represents the thickness of the damage region and an extremely sharp crack is obtained when  $c \rightarrow 0$ . A one dimensional visualization of the crack is seen in Figure (2.2). An accurate display of the use of the phase field can be observed in Figure (2.1). We also observe that the above equation is the solution of the differential equation:

$$c(x) - l^2 c''(x) = 0 \quad (2.7)$$

By using the principle of variations, we get the area of the broken material is obtained as:

$$\Gamma(c) = \frac{1}{2l} \int_{\Omega} (c^2 + l^2 c'^2) dV \quad (2.8)$$

Using Equation (2.8) in Equation (2.5) we obtain the new Lagrangian formation as :

$$L(\epsilon, \dot{u}, c) = a_{kin}(\dot{u}) - a_{pot}(\epsilon, c) - \int_{\Omega} [\frac{1}{2} \rho \dot{u}_i \dot{u}_i - a_e] dx - \frac{1}{2l} \int_{\Omega} G_c (c^2 + l^2 |\nabla c|^2) dV \quad (2.9)$$

### 2.1.3 Strain Energy

The strain energy density for the problem is given as:

$$a(\epsilon, c) = [(1 - c)^2 + k_r] a^+(\epsilon) + a^-(\epsilon) \quad (2.10)$$

Here  $a^+(\epsilon)$  consists of the strain energy that contributes to the damage while  $a^-(\epsilon)$  does not contribute to the damage. The  $k_r$  term is introduced to the equation for numerical stability. Various propositions for the decomposition of the strain energy has been made over the years for modelling damage in different materials. For our investigation four primary models have been used. Positive Volumetric Strain Model, Principal strain model [11], Amor model [12] and Symmetric model. Note that part of the strain energy that contributes to the damage is just  $a^+(\epsilon)$  because only that multiplies with the degradation function.

- **Positive Volumetric Strain Model**

$$a^+(\epsilon) = \frac{\lambda}{2} \langle tr(\epsilon) \rangle^2$$

$$a^-(\epsilon) = \frac{\lambda}{2} (tr(\epsilon) - \langle tr(\epsilon) \rangle)^2 + \mu tr((\epsilon^-)^2) \quad (2.11)$$

In this model the damage due to the degradation function is only associated with positive volumetric strain. So damage is only due to the tensile stresses in the material.

- **Principal Strain Model**

$$a^+(\epsilon) = \frac{\lambda}{2} \langle tr(\epsilon) \rangle^2 + \mu tr((\epsilon^+)^2)$$

$$a^-(\epsilon) = \frac{\lambda}{2} (tr(\epsilon) - \langle tr(\epsilon) \rangle)^2 + \mu tr((\epsilon^-)^2) \quad (2.12)$$

In this model the damage due to the degradation function is only associated with the positive principal strains. So damage is only due to tensile stresses and pure shear.

- **Amor Model**

$$\begin{aligned} a^+(\epsilon) &= \frac{\lambda}{2} \langle tr(\epsilon) \rangle^2 + \mu tr((\epsilon)^2) \\ a^-(\epsilon) &= \frac{\lambda}{2} (tr(\epsilon) - \langle tr(\epsilon) \rangle)^2 \end{aligned} \quad (2.13)$$

In this model the damage due to degradation is associated with the positive volumetric strain and complete deviatoric strain.

- **Symmetric Model**

$$\begin{aligned} a^+(\epsilon) &= \frac{\lambda}{2} tr(\epsilon)^2 + \mu tr((\epsilon)^2) \\ a^-(\epsilon) &= 0 \end{aligned} \quad (2.14)$$

In this model the damage due to degradation is associated with the total strain in material, be it tensile or compressive.

In the equations above  $\lambda$  and  $\mu$  denote the Lamé constants. The annotation  $\langle x \rangle$  is described as:

$$\langle x \rangle = \begin{cases} x, & x > 0 \\ 0, & x \leq 0 \end{cases} \quad (2.15)$$

The strain tensors used above are described as shown below in Equation (2.16) and Equation (2.17).

$$\epsilon^+ = \begin{pmatrix} \langle \epsilon_1 \rangle & 0 & 0 \\ 0 & \langle \epsilon_2 \rangle & 0 \\ 0 & 0 & \langle \epsilon_3 \rangle \end{pmatrix} \quad (2.16)$$

$$\epsilon^- = \begin{pmatrix} \epsilon_1 - \langle \epsilon_1 \rangle & 0 & 0 \\ 0 & \epsilon_2 - \langle \epsilon_2 \rangle & 0 \\ 0 & 0 & \epsilon_3 - \langle \epsilon_3 \rangle \end{pmatrix} \quad (2.17)$$

Here  $\epsilon_1, \epsilon_2$  and  $\epsilon_3$  denote the principal strains. The Equation (2.18) below makes sure of the irreversibility of the damage process, hence preventing healing of the damaged area.

$$\begin{aligned} \dot{W}_f \Gamma(c, \dot{c}) &= \int_{\Omega} G_c \dot{\gamma}(c, \nabla c) dV \geq 0 \\ \dot{\gamma}(c, \nabla c) &= \delta_c \gamma \dot{c} \geq 0 \end{aligned} \quad (2.18)$$

Using the regularized Lagrangian obtained in Equation (2.9) we obtain the coupled field equations including damage. Using the Euler Lagrange equation

$$-\frac{\partial a_e(\epsilon, c)}{\partial u} = \frac{d}{dt} \left( \frac{\partial a_{kin}(\dot{u})}{\partial \dot{u}} \right) \quad (2.19)$$

we get the equilibrium equation

$$\nabla \cdot \sigma = \rho \ddot{u} \quad (2.20)$$

The stress equation is given by

$$\sigma = \frac{\partial a(\epsilon, c)}{\partial \epsilon} = [(1 - c)^2 + k_r] \frac{\partial a^+(\epsilon)}{\partial \epsilon} + \frac{\partial a^-(\epsilon)}{\partial \epsilon} \quad (2.21)$$

Using the Euler-Lagrange equation

$$\frac{-\partial a_e(\epsilon, c)}{\partial c} - \frac{\partial a_f(c)}{\partial c} = 0 \quad (2.22)$$

we obtain

$$2(1 - c)a^+(\epsilon) = G_c \left( \frac{c}{l_0} - l_0 \nabla c \right) \quad (2.23)$$

For this work a rate dependent formation has been chosen, similar to that used in Grilli *et al.* [13] and Chakraborty *et al.* [14].

$$\dot{c} - \frac{1}{\eta} < l_0 \Delta c + 2(1 - c) \frac{a^+(\epsilon)}{G_c} - \frac{c}{l_0} > = 0 \quad (2.24)$$

Here a kinetic coefficient  $\eta$  has been introduced into the system that controls the rate of damage in the system as well as providing numerical stability to the system. It is also referred to as the viscosity parameter. The equation denotes a time dependent

Ginzburg-Landau evolution equation and are solved using their respective weak forms via a Finite Element method approach.

## 2.2 Frictional Heat Source

There are several mechanisms reported in literature than generate a large amount of heat due to impact loading on solid propellants. These include friction, plastic heating, void collapse, viscous heating etc. Out of all these mechanisms heating due to friction is considered to be dominant one as observed in Duarte et al. [15].

### 2.2.1 Numerical Model

The heat equation in its integral form is given as

$$\int_{\Omega} \rho C \frac{\partial T}{\partial t} dV = \int_{\Omega} \dot{q} dV - \int_{\partial\Omega} h \cdot ndA \quad (2.25)$$

Here  $T$  is the temperature,  $q$  is heat source density,  $C$  denotes specific heat capacity,  $k$  is the thermal conductivity and  $h = -k\nabla T$  denotes the heat flux per unit area across the surface  $\partial\Omega$ . The second term on the right hand side is further divided into two parts. One represents the domain boundary and one represents the crack surface.

$$\int_{\partial\Omega} h \cdot ndA = \int_{\partial\Omega-\Gamma} h_s dA + \int_{\Gamma} h_c dA \quad (2.26)$$

Here the  $h_s$  denotes the outward heat flux and  $h_c$  denotes the heat generated due to friction.  $h_c$  is calculated as

$$h_c = -\mu_s \langle -t_n \rangle v_s \quad (2.27)$$

Here  $\mu_s$  is the friction coefficient,  $t_n$  is the normal component of the traction vector. The angular bracket ensures that heat is generated only when the cracks are closed (i.e. Negative traction).  $v_s$  represents the magnitude of the sliding velocity and is

assumed as the tangential component of the velocity jump between the two crack surfaces. it is approximated as

$$\mathbf{v} = l_o v_{i,j} n_j \quad (2.28)$$

where the  $l_o$  denoted the characteristic length as shown in Equation (2.6). The normal to the crack surface is calculated using the phase field parameter as

$$\mathbf{n} = -\frac{\nabla c}{|\nabla c|} \quad (2.29)$$

All the simulations have been carried out using a Phase Field Damage model implementation in MOOSE (Multiphysics object oriented simulation environment) framework [16]. The model employs an explicit solver which is based on the Newmark time intergration scheme.

### 3. MODEL VALIDATION AND ANALYSIS

#### 3.1 Introduction

A quantitative rate dependent phase field model approach has been employed to study the complex crack propagation behaviour of a brittle material. Here we investigate and validate our model using Mode-I fracture of a PMMA rectangular plate. Similar geometry has been analyzed experimentally and will be extremely useful in validating our model. From the experimental conclusions mentioned in the experiment conducted in Zhou *et al.* [7] it has been observed that depending on the loading conditions the crack tip velocity ( $v_o$ ) varies from 0-650 m/s. Lower velocities denote a stable crack growth while at higher velocities ( $v_o > \approx 650$  m/s) certain crack show unstable growth and leads to crack branching.

#### 3.2 Simulation Setup

A 2D domain with plain strain assumption is used for the simulation with an effort to duplicate a Mode 1 displacement controlled setup. The initial crack length in the simulation is taken as  $a = 8mm$ . The crack is represented using a phase field parameter  $c$ .  $c=1$  at the center of the crack and slowly diffuses to  $c=0$  as we move away from the crack. The exact domain used for the simulation is as shown in Figure (3.1). The primary domain employed for the study consists of around 20000 square elements. The left and the right boundaries are free and a displacement controlled loading condition is applied on the top and the bottom boundary.

In the experimental setup used in Zhou *et al.* [7] a displacement is applied to the top and the bottom boundary of the rectangular plate in a quasi-static manner until the desired displacement is reached. A sharp crack is then produced and a steady-state

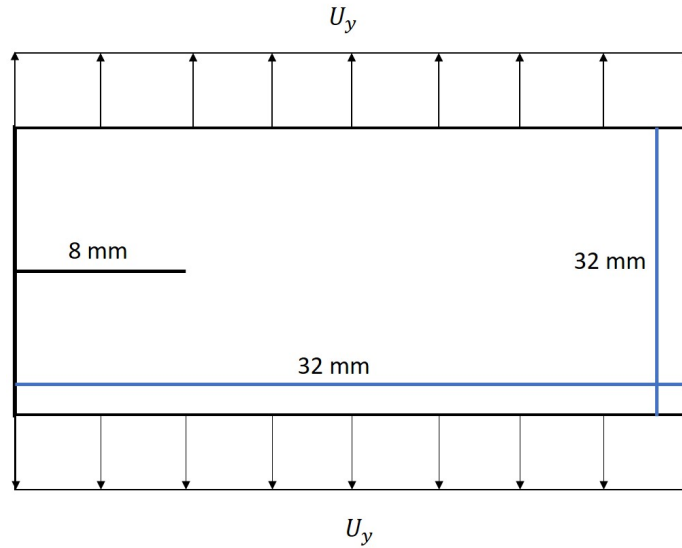


Fig. 3.1. Domain employed in the Mode-1 displacement control simulations.

Table 3.1.  
Material properties used in the simulations [17–19].

Property	PMMA
E [GPa]	3.09
$\nu$	0.35
$G_c$ [J/m <sup>2</sup> ]	300
$\rho$ [kg/m <sup>3</sup> ]	1180

crack propagation is observed. Due to this the crack propagation is easily observed and also the stored energy of the system can be easily defined. So as to replicate the phenomena the domain is pre-strained first by applying the displacement to the domain using a quasi-static simulation. Subsequently a dynamic simulation is applied for the crack growth and branching phenomena.

The material properties used in the simulations are given in Table (3.1). An important assumption here is that PMMA is considered to be isotropic linear elastic in the simulations.

Table 3.2.  
General mesh parameters employed in the simulations.

Parameter	Value
$h$ [Element size]	$160\mu m$
$l_o$ [Length Scale]	$800\mu m$

The numerical parameters used in the simulation are given in Table (3.2). The reason as to why the particular values have been chosen are explained in the subsequent chapters. Other numerical parameters employed in the simulation are  $k_r = 1 \cdot 10^{-6}$ . This ensures numerical stability as mentioned in Equation (2.10). The viscosity parameter used in most simulations is given as  $\eta = 0.1 \text{ s/m}$ . The constants used for the Newmark integration scheme are  $\beta = 0.3025$  and  $\gamma = 0.6$ . The timestep used for the simulation is  $\Delta t = 10ns$ .

For the crack tip velocity calculations a code has been written in such a way that the top-right element with the  $c > 0.9$  is tracked. It is implied that if the crack branches only the top branch is considered for the crack tip velocity calculation.

### 3.2.1 Mesh Sensitivity Analysis

For the mesh sensitivity analysis, the same domain as shown in Figure (3.1) was used. Three different mesh with element size  $h = 320 \mu m$ ,  $h = 160 \mu m$  and  $h = 80 \mu m$  were used. All the other material and numerical parameters were kept the same. The length scale parameter followed the same rule for all the three meshes i.e.  $l_o = 5h$ . A displacement of  $\Delta U = 120\mu m$  was applied quasi-statically to all the three meshes and subsequently dynamic simulations were run for the crack propagation analysis.

In Figure (3.2) the damage field can be seen for the three different set-ups. It can be observed that crack is more prominently defined as we decrease the size of the mesh. As mesh size is increased the diffusion of the damage field is also increased which leads to lesser resolution of the crack surface. The evolution of the crack tip

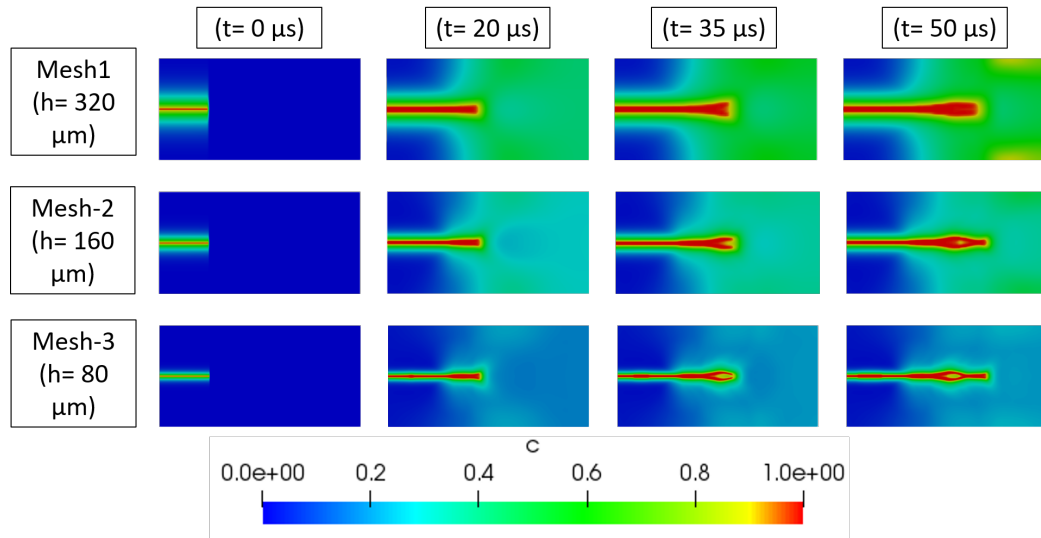


Fig. 3.2. Phase field damage field for the same domain with varying element size.

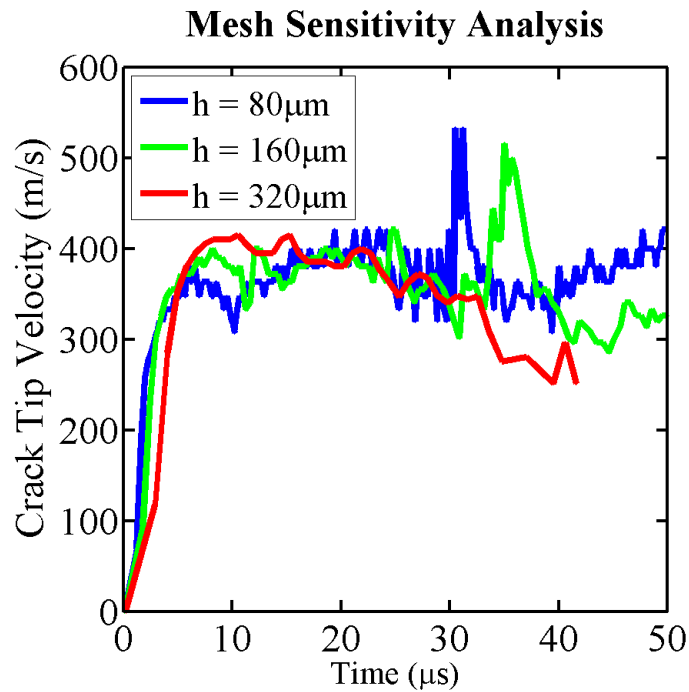


Fig. 3.3. Evolution of the crack tip velocity for three different mesh sizes.

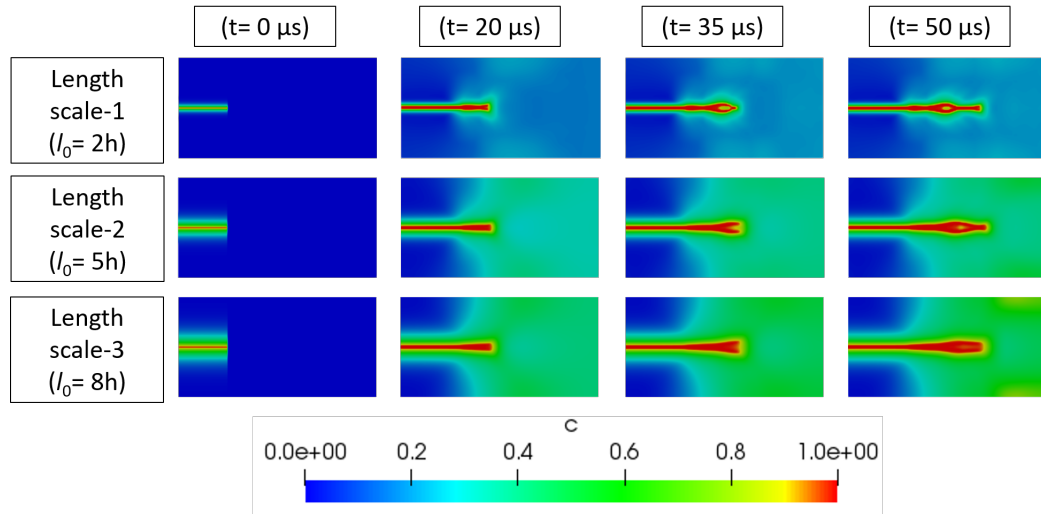


Fig. 3.4. Phase field damage field for three varying length scale parameters.

velocity is shown in Figure (3.3). From the figure it can be seen that the crack velocity lies in the same range for all the three different meshes. However the branching phenomena is observed in the two meshes with smaller element sizes and occurs when the crack tip velocity reaches a range of 520-600 m/s. The simulation with the largest element size does not undergo branching and just a widening of the crack is observed. Hence it is pivotal that the mesh chosen suffices the dual criteria of resolution as well as computational optimization.

### 3.2.2 Length Scale Parameter Analysis

For the same mesh three different length scales were analyzed.  $l_o = 2h$ ,  $l_o = 5h$  and  $l_o = 8h$ . All the other material and numerical parameters were kept the same. The damage field can be observed from Figure (3.4). It can be observed that the length scale parameter behaves analogous to the behaviour seen for mesh sensitivity analysis. For higher length scales there is higher diffusion which leads to loss of important features. Taking higher length scales is also impractical from a physical point of view as cracks are sharp discontinuities and not diffused. However from a numerical point of

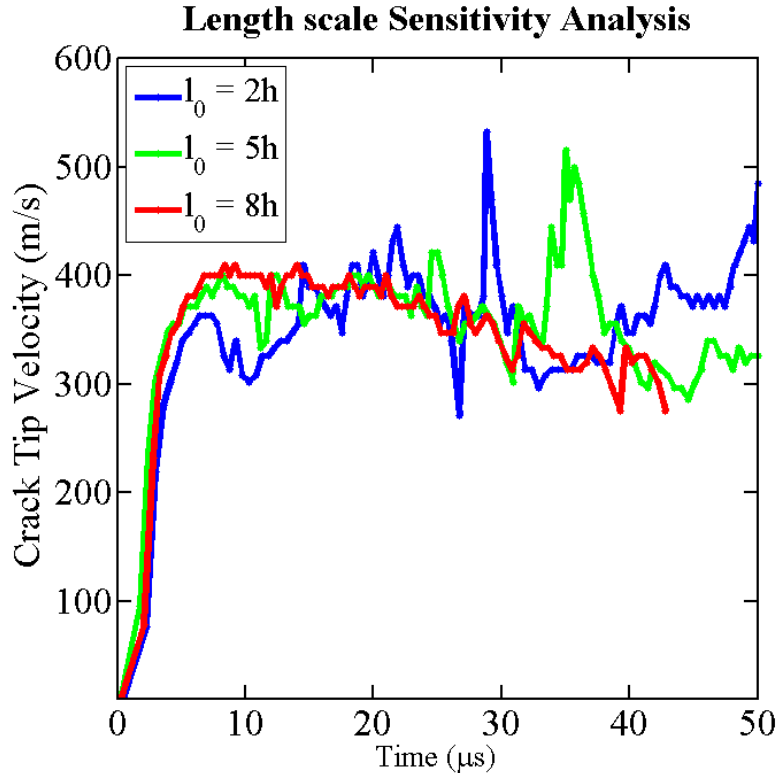


Fig. 3.5. Evolution of the crack tip velocity for three varying length scale parameters.

view taking extremely short length scales are also disadvantageous. It has been shown in literature that as we decrease the length scale the fracture energy overestimated is increased [20]. Hence with this point of view higher length scales are preferred. So an optimized length scale should be considered. From Figure (3.5) it can be seen that the crack tip velocities for all the three length scales lies in the same range however when  $l_o = 8h$  the crack does not accelerate enough for a branching phenomena.

### 3.2.3 $\eta$ Parameter Analysis

The  $\eta$  parameter also referred to as the viscosity parameter controls the rate at which damage propagates. Hence it is a vital parameter that controls the crack tip velocity. In Figure (3.6) the variation in the crack tip velocity with respect to varying

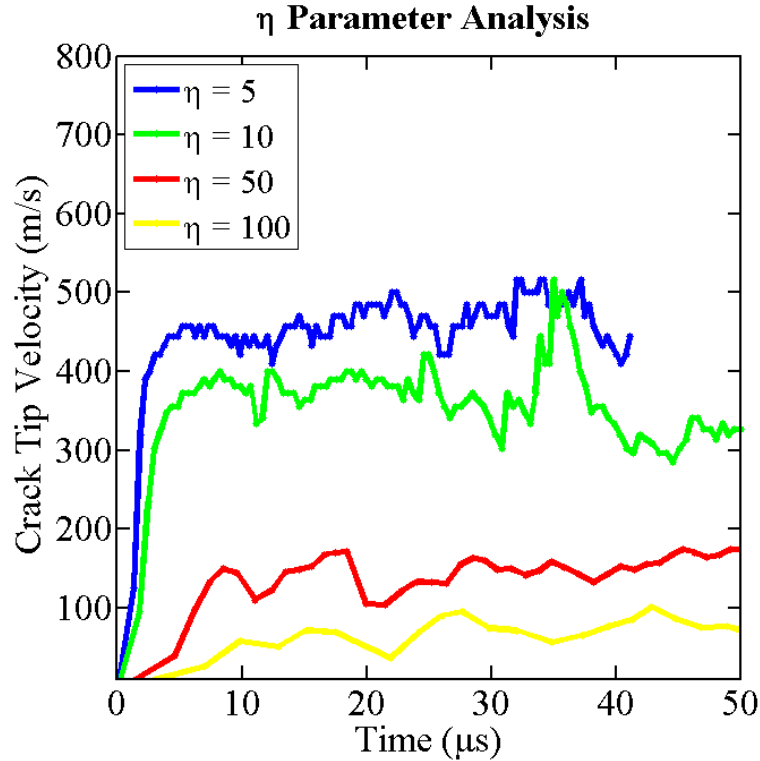


Fig. 3.6. Evolution of the crack tip velocity for three varying length scale parameters.

viscosity parameters is shown. It can be seen that with increase in the value of the viscosity parameter the crack tip velocity decreases significantly. Hence a value of  $\eta = 10 \text{ ns}/\mu\text{m}$  is chosen as it gives a crack tip velocity which is close to the value obtained in the experiments reported in literature. [7,18,19,21,22]

### 3.2.4 Results for Multiple Loading Conditions

After choosing the desired values for the multiple numerical and material parameters, analysis was performed for various displacement loading conditions. Primarily four values were chosen.  $\Delta U = 100\mu\text{m}$ ,  $\Delta U = 120\mu\text{m}$ ,  $\Delta U = 140\mu\text{m}$  and  $\Delta U = 160\mu\text{m}$ . The results for the same are as shown in Figure (3.7). The crack tip velocities for the different loading conditions can be seen in Figure (3.8). For reference

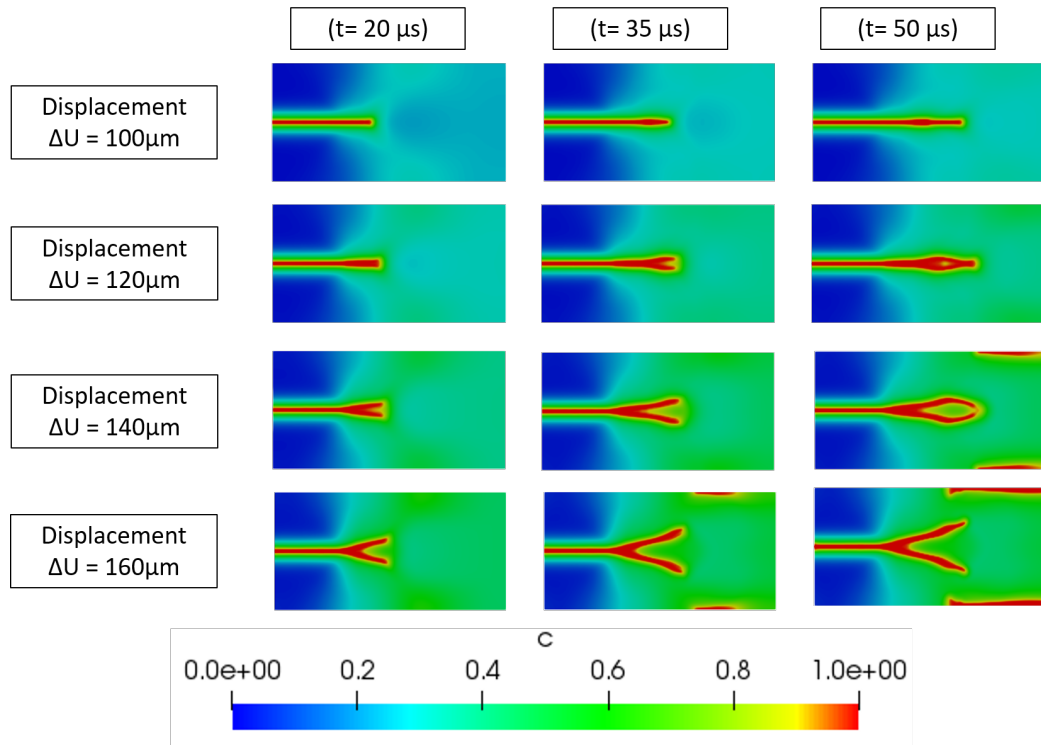


Fig. 3.7. Evolution of the crack tip for four varying displacement conditions. The mesh parameters used are  $h = 160\mu m$ ,  $l_o = 5h$  and  $\eta = 10ns/\mu m$ .

a horizontal line has drawn which represents the velocity at which crack branching is observed in the experiments. It is represented as  $0.67C_r$ .  $C_r$  is the Raleigh wave speed of the material and is calculated to 906 m/s for PMMA.

The arrows in Figure (3.8) represent the limiting velocity at which branching occurs. For higher displacement we observe that the velocity constantly increases up to a point where a single crack cannot be sustained and branching is observed. We can see that branching for the simulations occur at velocities close to  $0.67C_r$ . Higher displacements lead to unstable crack growth and hence higher fluctuations are observed. For  $\Delta U = 100\mu m$  no branching is observed as evident from Figure (3.7) hence no spike in velocity is seen in Fig (3.8).

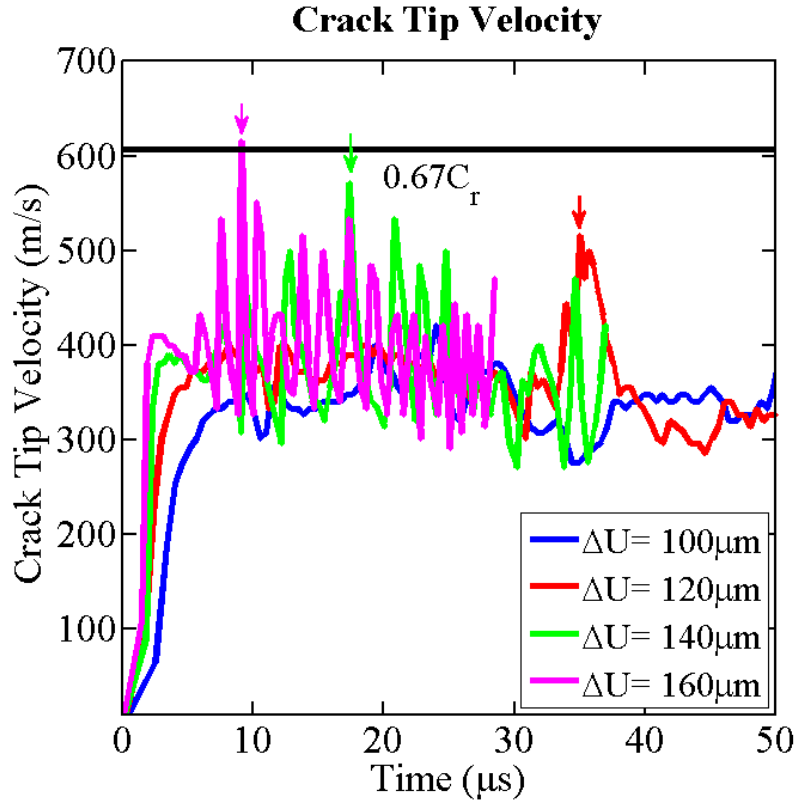


Fig. 3.8. Evolution of the crack tip velocity for four varying displacement loading conditions.

### 3.3 Summary

In the experiments conducted by Zhou *et al.*, a PMMA plate is clamped on both the sides by heavy grips. After reaching a given load a sharp crack is induced using a razor and the crack propagates straight across the specimen. These are performed for varying initial loads and the velocity of the crack tip is measured in each case. The experiment results are as observed in Figure 3.9.

From the experiments above few conclusions have been drawn. At a low crack tip velocities ( $v_o < 200\text{m/s}$ ) the fractured surface found is very smooth. In the approximate velocity range of  $200\text{m/s} < v_o < 450\text{m/s}$  there are parabolic geometrical patterns observed. At higher velocity range of  $480\text{m/s} < v_o < 600\text{m/s}$  periodic stria-

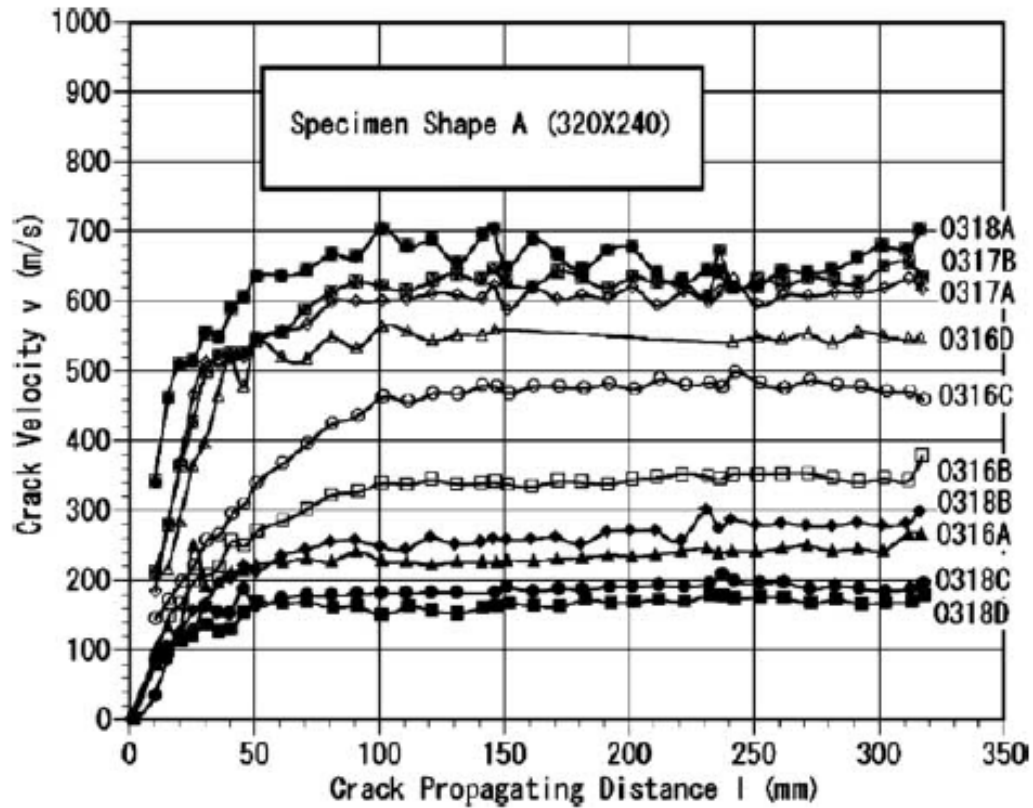


Fig. 3.9. The plot of crack velocities for different samples obtained from Zhou *et al.* [7].

tions are observed and it increases with the increase in velocity. The crack growth in this case is considered to be unstable in a local sense. When the crack velocity exceeds a value of  $600\text{m/s}$  micro-cracks develop from the main crack and these micro-cracks have a possibility of propagating which leads to the phenomenon of branching.

In the simulation above a similar setup as seen in the experiments has been used. A parametric analysis of the numerical parameters and its effect on the crack tip velocity has also been studied. We observe stable crack growth at lower loading displacement and unstable crack growth with high velocity fluctuations at higher

loading displacements. We also find that the crack accelerates up to a value of  $0.67C_r$  before branching. Also in some cases that even though the crack attempts to branch the energy is not enough for sustenance of two cracks and hence they combine again for a single crack growth. This is a behaviour which is very similar as seen for cracks in the periodic striation regime. Hence the simulations performed show a reasonable acceptance with the experiments performed. Hence the phase field approach used proves to be an effective model to study the complex system of dynamic fracture. Although the model is effective in reproducing the experimental data many questions still exist. A deeper study pertaining to stress intensity factors and energy release rate with respect to crack branching phenomena still needs to be assessed.

## 4. THERMAL-MECHANICAL ANALYSIS OF PBX MICROSTRUCTURES

Computational simulation of single energetic crystals embedded in binder are widely abundant in literature [13, 15, 23]. The production crystals usually employed tend to have smaller crystals and contains defects. These defects are extremely pivotal as it severely effects the behavior of the material. So for the given chapter a real microstructure has been chosen and using it as a reference a mesh has been created to stochastically analyze how random crack patterns inside the crystals affect its behavior. Several loading velocities and multiple  $G_c$  have been chosen to study the damage pattern and the temperature increase inside the particle with friction being the heat source. Several attempts have been made in previous literature to study the affects of PBX via a microstructural mesh. A varying volume fraction of HMX crystals have been introduced up to a volume fraction of 82 % inside a binder to study its affect on the PBX [24, 25]. In this study one such PBX has been chosen which contains 91% HMX and 9% Sylgard by volume. The mesh was prepared using digitization of the SEM image of an EDC 37 crystal.

### 4.1 Simulation Setup

To simulate a particle dense microstructure, a part of the microstructure with a dimension of 200 micron x 150 micron has been chosen as seen in Figure (4.1). The area for this has been chosen so as to capture the maximum details pertaining to the particles. A mesh has been prepared using digitization, following a similar geometry to that of the selected area. A volume fraction of 79% HMX and 21% Sylgard has been obtained. This is not the ideal volume fraction for the PBX that is desired. This is one of the shortcomings of digitization. A mesh has been made using triangular

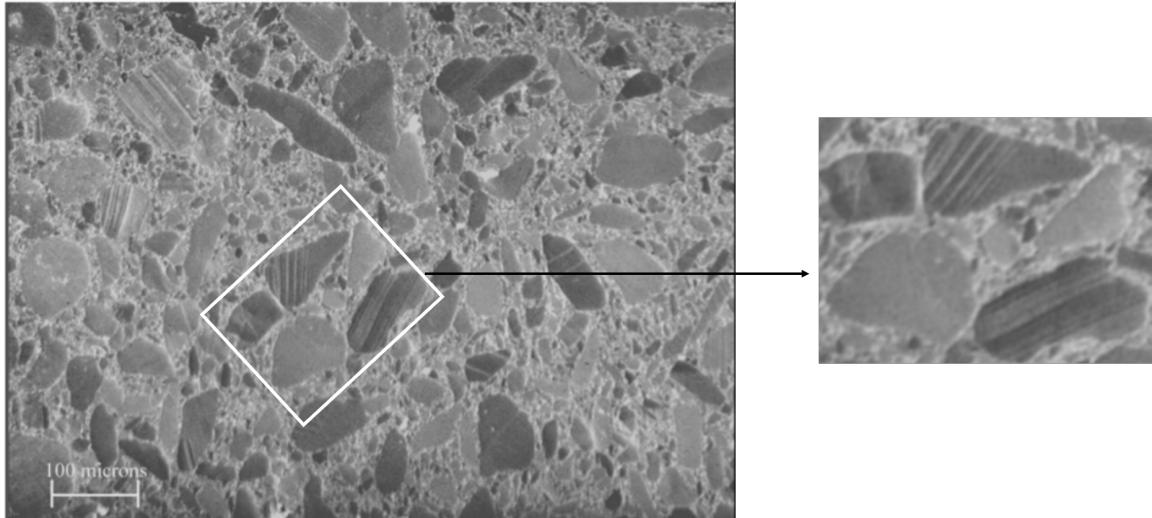


Fig. 4.1. The micro-structure [26] and the adopted area for mesh generation.

elements with an average size of  $1 \mu m$ . The mesh has over 90000 elements. The given geometry has been subjected to various compressive loading velocities of 10 m/s, 50 m/s and 100 m/s. For this geometry we assume a plane strain formulation. It is important to know that the binder follows the principal strain model and the HMX crystals follow the Miehe strain formulation. It is important to know that to both the particle and binder the damage is observed only under tensile stresses (Positive Eigen strains).

As seen in Figure (4.2) periodic loading conditions have been applied to the top and the bottom boundaries and a Dirichlet displacement boundary condition has been applied to the left boundary. The right boundary is fixed in the X direction and free in the Y direction. In these simulations periodic boundary conditions have been applied because we are analyzing a sub-domain in a given image assuming an infinite domain. The simulation is dynamic in nature. The material properties used are as shown in Table (4.1). Mesh parameters employed are as shown in Table (4.2).

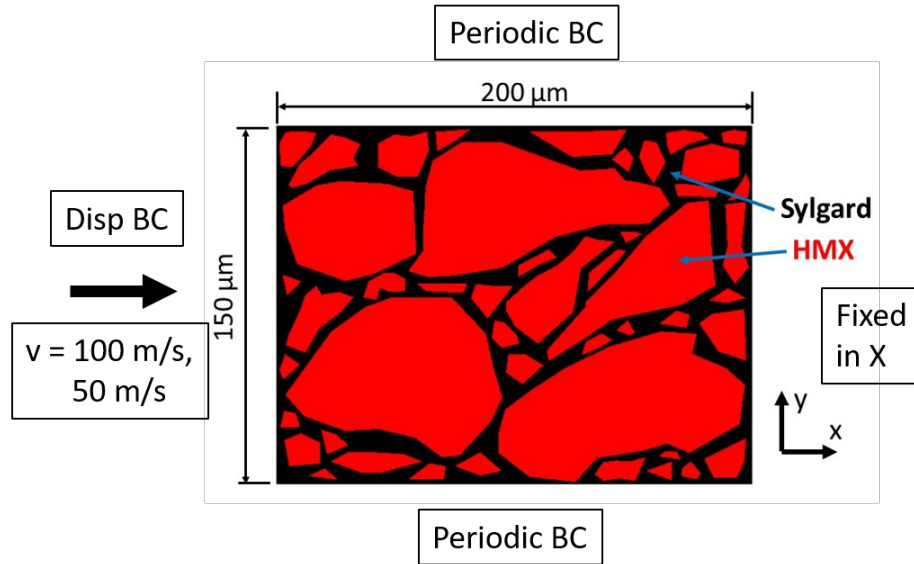


Fig. 4.2. The domain generated after digitization depicting the type of boundary and loading conditions used.

Table 4.1.  
Material properties used in the simulations [27–31].

Property	HMX	Sylgard
$E$ [GPa]	15	0.15
$\nu$	0.35	0.48
$G_c$ [J/m <sup>2</sup> ]	2	400
$\rho$ [kg/m <sup>3</sup> ]	1903	1030
$T_{initial}$ [K]	300	300
$k$ [W/m.K]	0.31	0.18
$c_p$ [J/kg.K]	1200	1100

Table 4.2.  
Mesh parameters employed in the simulations.

Parameter	Value
$h$ [Element size]	$1\mu m$
$l_o$ [Length Scale]	$4\mu m$

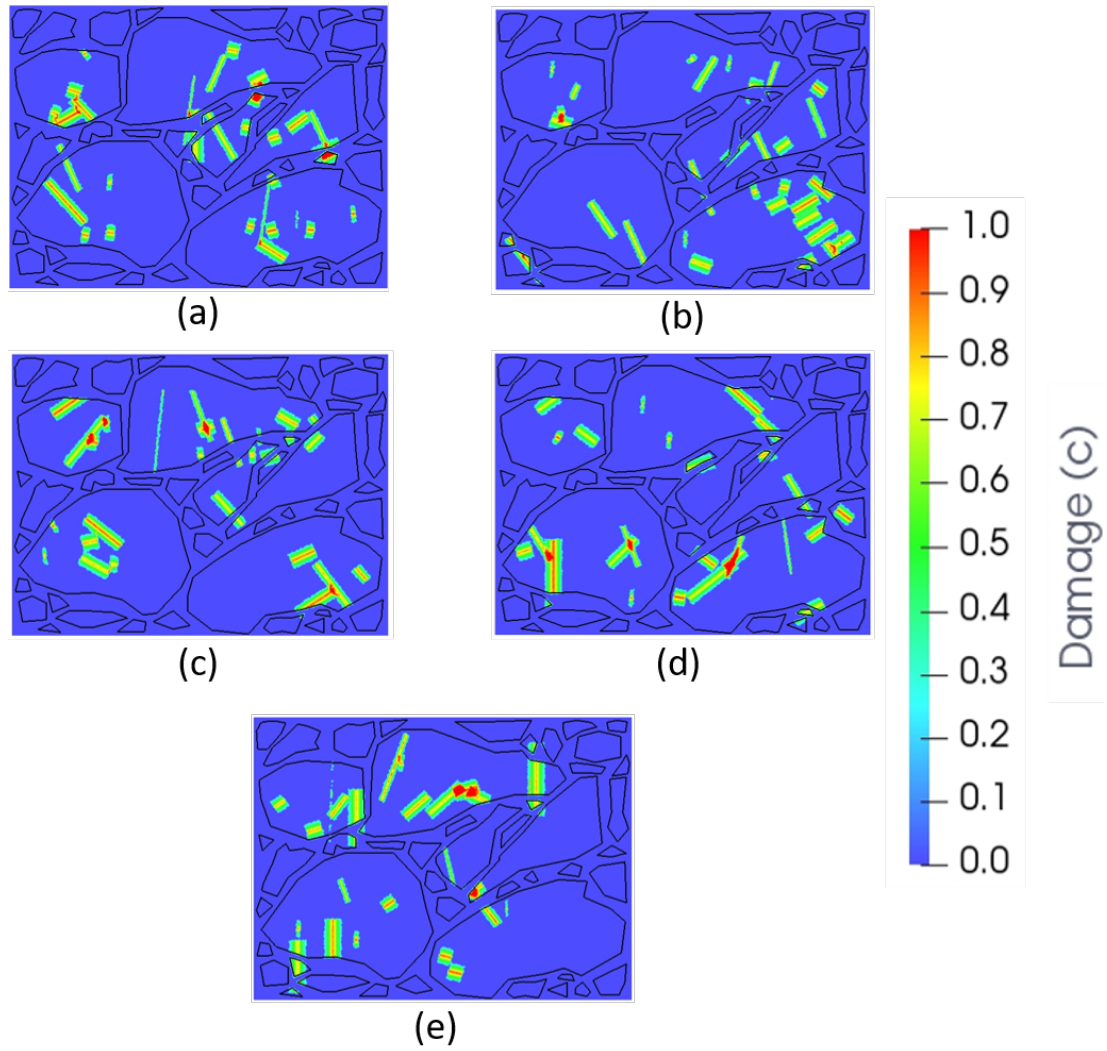


Fig. 4.3. The varying crack distributions used. (a) Crack Distribution-1 (b) Crack Distribution-2 (c) Crack Distribution-3 (d) Crack Distribution-4 (e) Crack Distribution-5. Initial crack density  $\rho = 5\%$  ; Mean crack length =  $12.5\mu m$  and a Standard Deviation in the crack length =  $5\mu m$ .

Other numerical parameters used are  $k_r = 1 \cdot 10^{-6}$  and  $\eta = 0.01 \text{ s/m}$ . The constants used for the Newmark integration scheme are  $\beta = 0.3025$  and  $\gamma = 0.6$ . For the given geometry artificial cracks have been added to the system in the form of phase field cracks. Five such distributions have been analyzed with Initial crack density  $\rho = 5\%$ . The crack length follow a Gaussian distribution a mean of  $12.5\mu\text{m}$  and a Standard Deviation of  $5\mu\text{m}$ . The five random distributions can be seen in Figure (4.3).

## 4.2 Damage Evolution

For this study two primary critical energy release rates were chosen i.e.  $G_c = 2$  and  $G_c = 0.12$ . In literature the value of the fracture surface energy obtained via the Vickers harness test was found to be  $\gamma = 0.06\text{J/m}^2$  as seen in Palmer *et al.* [32]. The value of  $G_c = 2$  was chosen so as to account for the formation of plastic zone around the crack tip which leads to stress relaxation. The simulations for velocities of  $100\text{m/s}$  and  $50\text{m/s}$  are performed in such a way that the loading is applied till the stress wave reaches the end of the domain. In these cases the first wave pass takes 100 ns to reach the end of the domain. The first wave pass can be seen in Figure (4.4). The stress in the figure is represented by von Mises stress. The damage at the end of the first wave pass can also be seen. Both the simulations have an impact velocity of  $100\text{m/s}$ . It can be observed that there is hardly any damage at the end of the first wave pass as seen in Figure (4.4(a)) while the simulation with  $G_c = 0.12\text{J/m}^2$  shows considerable damage. It is also important to note that cracks in the particle that are close to the interface tend to grow faster. Also crack growth is affected significantly by stress concentration areas in the system. However, depending on the critical energy release rate of the system the rate of damage can significantly increase or decrease.

In Figure (4.5).the effect on damage field due to the varying velocities can be observed. Both the simulations shown have the same critical energy release rate i.e.  $G_c = 0.12\text{J/m}^2$ . It is evident that even at the same strain the simulation with higher

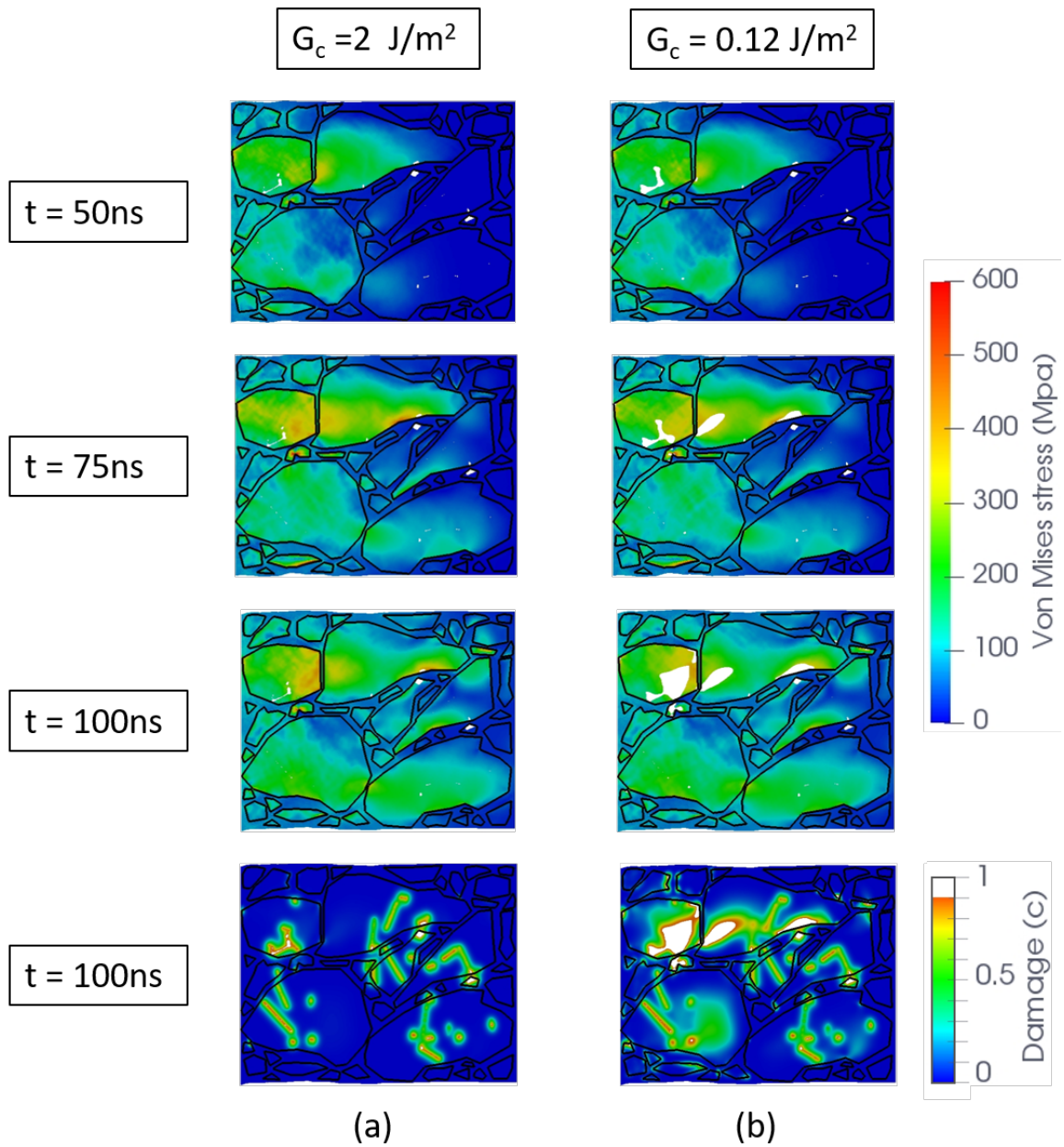


Fig. 4.4. Damage field and von Mises stress field plots for distribution-1. (a)  $G_c = 2\text{J/m}^2$ ;  $v = 100\text{m/s}$  (b)  $G_c = 0.12\text{J/m}^2$ ;  $v = 100\text{m/s}$ . Please note that the nodes with  $c > 0.9$  have been removed for the Von-mises stress plots.

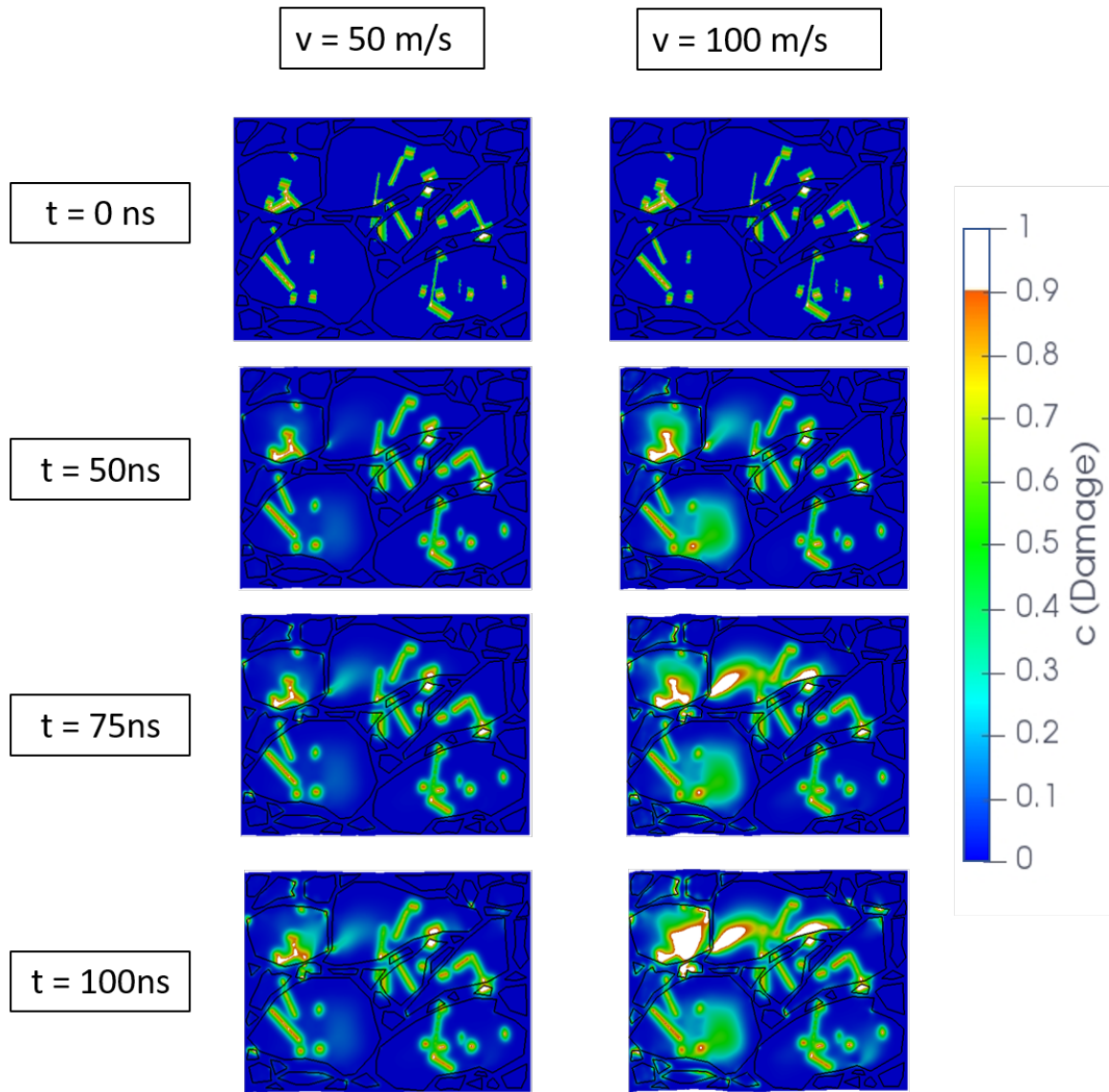


Fig. 4.5. Damage field plots of distribution-1 for loading velocity comparison. (a)  $G_c = 0.12 \text{ J/m}^2$ ;  $v = 50 \text{ m/s}$  (b)  $G_c = 0.12 \text{ J/m}^2$ ;  $v = 100 \text{ m/s}$ .

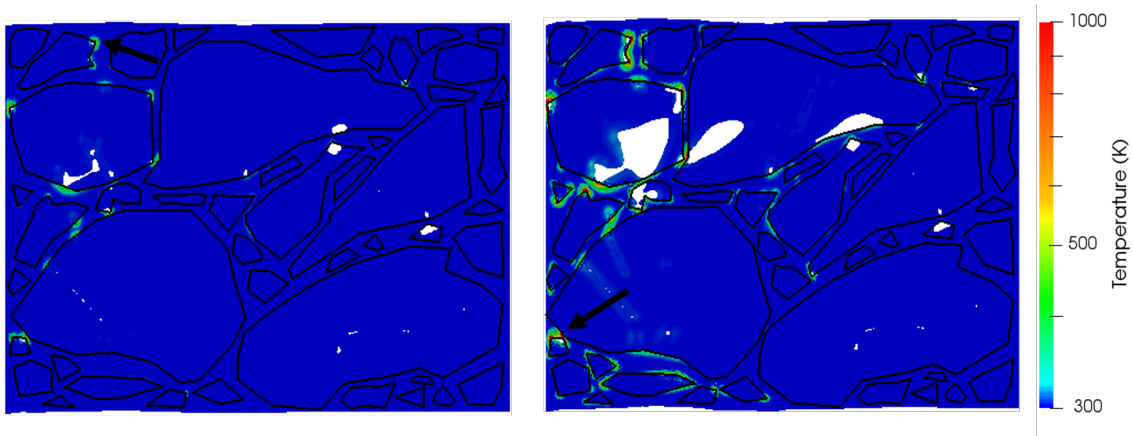


Fig. 4.6. Temperature field for distribution1.(a)  $t = 100ns$ ;  $v = 50m/s$  (b)  $t = 100ns$ ;  $v = 100m/s$ . The arrows indicate the hotspot with the maximum temperature. Please note that nodes with  $c > 0.9$  have been removed.

loading velocity shows greater damage. This is attributed to the higher strain rate in the system which causes higher strain amplitudes.

### 4.3 Temperature Evolution

The temperature rise in the system is obtained according to the model described in Section 2.2 with friction being the only heat source in the system. The representative contour plots for  $v = 50m/s$  and  $v = 100m/s$  are as shown in Figure (4.6). Both simulations have the same critical energy release rate and strain. The arrows represents the area with the highest temperature rise in the system. It is important to note that temperature increase on the left boundary is not taken into consideration. It is observed in all the cases that temperature rise in prevalent at the interface between the polymer and HMX.

For a stochastic analysis, the average temperature over an area of radius  $R = 2 \mu m$ , where the highest temperature increase occurs is plotted against time. The plots for the same can be seen in Figure (4.7). It can be observed that for a critical energy

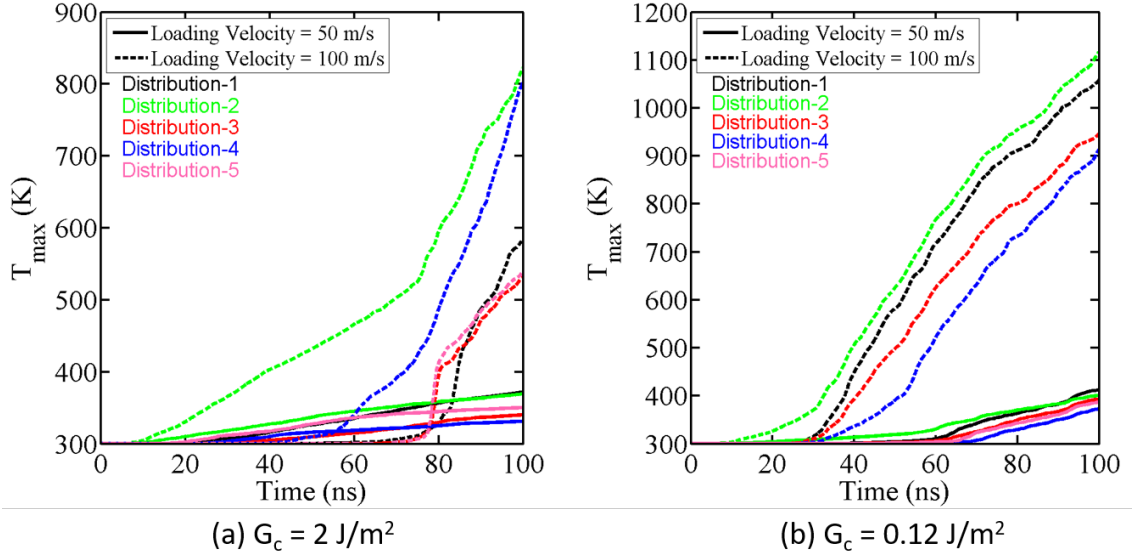


Fig. 4.7. Temperature-time evolution plots for the hotspot with the maximum temperature.

release rate of  $G_c = 2 \text{ J/m}^2$  and loading velocity of  $v = 100 \text{ m/s}$  and five different orientations a variation of  $\Delta T = 280 \text{ K}$  is observed as evident in Figure (4.7.(a)) for the last time step. For  $G_c = 2 \text{ J/m}^2$  and  $v = 50 \text{ m/s}$  a variation of  $\Delta T = 50 \text{ K}$  is observed. Similarly for a critical energy release rate of  $G_c = 0.12 \text{ J/m}^2$  a variation of  $\Delta T = 200 \text{ K}$  and  $\Delta T = 50 \text{ K}$  can be observed respectively. It can also be observed that a lower value of the critical energy release rate leads to higher damage and higher temperature increase in the system.

A similar study for a loading velocity of  $v = 10 \text{ m/s}$  has also been performed, however these simulation have been performed for a longer duration for appropriate strains. The temperature plots for such can be observed in Figure (4.8). The value of the energy release rate used for this simulation is  $G_c = 0.12 \text{ J/m}^2$ . A variation of  $\Delta T = 210 \text{ K}$  can be observed in this system itself. The temperature time increase rate for the given simulations are in the order of  $\approx 10^{10} \text{ K/s}$ . This is a reasonable value as it lies between the range of  $10^6$  and  $10^{12} \text{ K/s}$  as observed in literature [33–35].

Lower limit is seen for a vibration loading regime and the upper limit is seen for the shock regime.

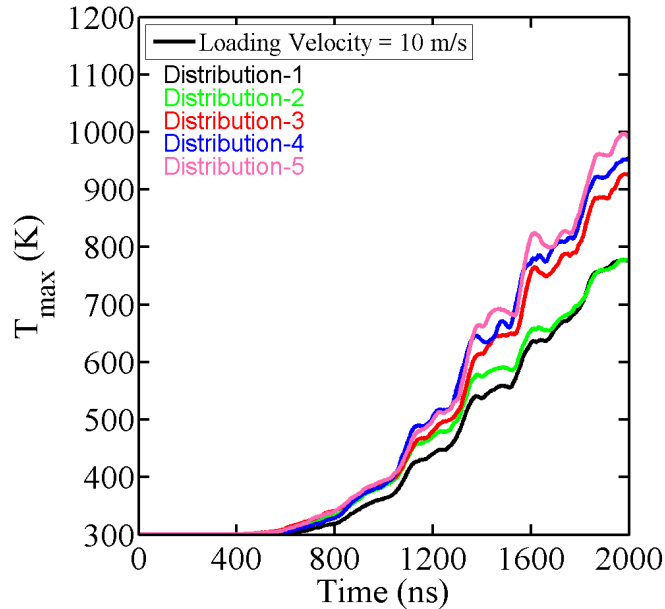
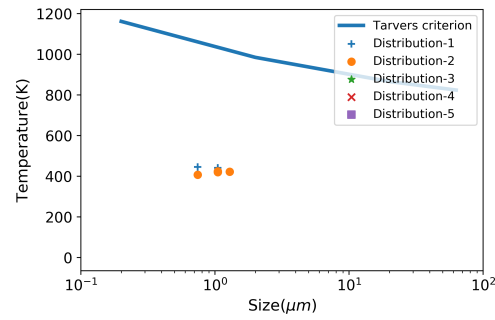


Fig. 4.8. Temperature-time evolution plots for the hotspot with the maximum temperature.

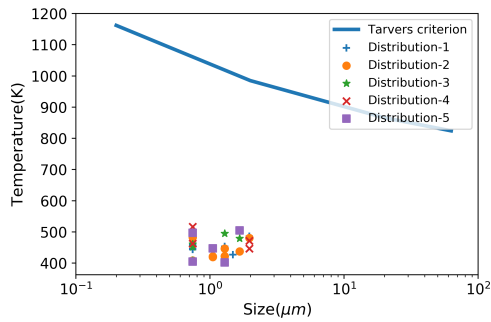
A conclusion can be made that the damage and temperature evolution is affected to a significant degree depending on the artificial defects introduced to the system. For the same crack density introduced to the system; varying crack length, orientation and positioning play an important role in determining the damage and temperature field of the system.

#### 4.4 Cluster Analysis for Hotspot Initiation

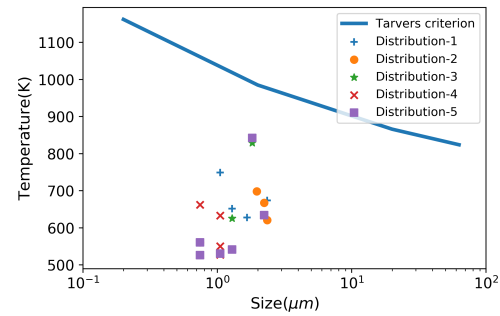
A hierarchical clustering method has been used to determine the hot spot formation in the system. The plots for the same can be seen in Figure (4.9). The data for the critical hotspots that may lead to initiation has been obtained from Tarver *et al.* [36]. Any hotspot that lies above the Tarver criterion will lead to initiation. It is evident from the figure that critical hotspots are found only in one case i.e. Figure



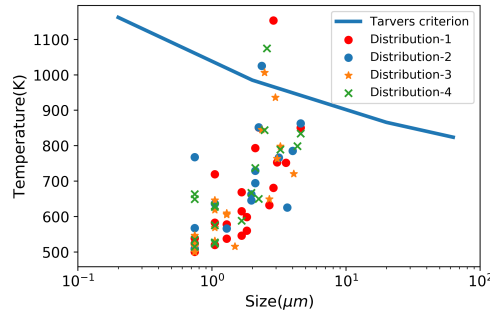
(a)



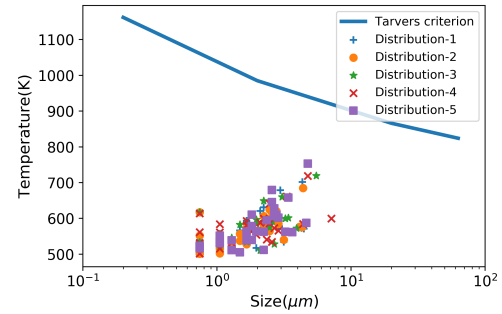
(b)



(c)



(d)



(e)

Fig. 4.9. (a)  $G_c = 2J/m^2$  ;  $v = 50m/s$  (b)  $G_c = 0.12J/m^2$  ;  $v = 50m/s$  (c)  $G_c = 2J/m^2$  ;  $v = 100m/s$  (d)  $G_c = 0.12J/m^2$  ;  $v = 100m/s$  (e)  $G_c = 0.12J/m^2$  ;  $v = 10m/s$ . Hotspot temperature and size for various impact velocities and critical energy release rates.

(4.9(e)). Thus it can be said that for  $G_c = 0.12J/m^2$  and a loading velocity of  $100m/s$  initiation will occur. A similar trend has also been observed in the low impact ex-

periments conducted by Idar *et al.* [37]. In the experiment an impact ranging from  $20\text{m/s} - 100\text{m/s}$  is conducted. Violent chemical reactions are observed for an impact velocity of above  $70\text{ m/s}$ .

#### 4.5 Dirty Binder

The aim of multiscale modeling of the materials is to predict its behaviour at different length scales. The length scale can vary from an atomistic to a macroscopic approach. In the simulations above the mesh contains 79% HMX and 21% Sylgard. Now the volume fraction of HMX is considerably low as compared to production PBX 9501 which contains 91% HMX by volume. So as to bridge this gap we assume that there are submicron particles in the binder which constitute for the missing 11 % of the HMX. These submicron particles do not undergo fracture and simply modify the material properties of the binder. In other words we are assuming that the binder with the smaller particles can be represented as a continuum using homogenized properties so as to explicitly represent the larger particles. A similar approach has been used in Xue *et al.* [38] and in Banerjee *et al.* [39].

To find the modified properties of the binder simple mixture rules have been used. To find the effective properties of the system we use Rule of mixtures. The modified properties used can be seen in Table ( 4.3).

The equation used to calculate the upper limit of the Young's modulus is given as:

$$E_1 \cdot f_1 + E_2 \cdot f_2 = E_{eff} \quad (4.1)$$

In the equation above  $E$  denotes the Young's modulus and  $f$  denotes the volume fraction. The subscript 1 and 2 denotes the materials used for the composite while the subscript  $eff$  denotes the effective material obtained.

For the lower limit of the Young's modulus the following equation is used:

Table 4.3.  
Material properties used in the simulations.

Property	HMX	Sylgard	Dirty Binder (Lower limit)	Dirty Binder (Upper limit)
$E$ [GPa]	15	0.15	0.38	9.35
$\nu$	0.35	0.48	0.399	0.399
$G_c$ [J/m <sup>2</sup> ]	2	400	400	400
$\rho$ [kg/m <sup>3</sup> ]	1903	1030	1569	1569
$T_{initial}$ [K]	300	300	300	300
$k$ [W/m.K]	0.31	0.18	0.243	0.243
$c_p$ [J/kg.K]	1200	1100	1175	1175

$$\frac{f_1}{E_1} + \frac{f_2}{E_2} = \frac{1}{E_{eff}} \quad (4.2)$$

Note rule of mixtures is an approximation that gives us an upper and lower bound of the property. The actual value of the property can be any value between the two bounds found from the rule of mixtures.

The equation for density is given as:

$$\rho_1 \cdot f_1 + \rho_2 \cdot f_2 = \rho_{eff} \quad (4.3)$$

In the equation above  $\rho$  denotes the density of the material. The equation for Poisson's ratio is given as:

$$\nu_1 \cdot f_1 + \nu_2 \cdot f_2 = \nu_{eff} \quad (4.4)$$

Here  $\nu$  denotes the Poisson's ratio. Thermal conductivity is calculated using:

$$\frac{f_1}{k_1} + \frac{f_2}{k_2} = \frac{1}{k_{eff}} \quad (4.5)$$

Here  $k$  is the thermal conductivity of the material We equate energy for calculating the effective specific heat capacity and the equation is given as:

$$\rho_1 \cdot f_1 \cdot C_1 + \rho_2 \cdot f_2 \cdot C_2 = \rho_{eff} \cdot C_{eff} \quad (4.6)$$

Here  $C$  denotes the specific heat capacity.  $\rho_{eff}$  is obtained from Equation (4.3).

The rule of mixtures is a crude way of approximating the material properties of a composite. This gives an effective range of the material properties. So simulations will further be performed within this range to determine the behaviour of the material with these varying properties. Using this a more realistic behaviour of the material can be obtained.

## 4.6 Summary

For the microstructure, a domain with HMX as an energetic and Sylgard as the matrix has been analyzed. The domain has a high grain volume fraction of 0.79. Artificial cracks have been introduced in the system in the form of phase field cracks. The five distributions have a crack density of 5% with the crack length following a Gaussian distribution with a mean of  $12.5\mu m$  and a standard deviation of 5. Impact velocities ranging from 10m/s-100m/s have been applied to the system. We observe that for higher velocities the fracture energy dissipated is higher near the impact surface which tends to show higher damage and temperature. The effect of critical energy release rate on the damage and temperature field has also been studied. For lower values of  $G_c$  temperature increase and damage observed is high. Also depending on the crack distributions the maximum temperature is found to be highly stochastic and reach up to approximately 900K - 1100K for a loading velocity of 100 m/s. Hence for such temperature rise, critical hotspots that may lead to initiation is a possibility. This agrees with the low impact simulations as shown in Idar *et al.* [37]. Thus a stochastic analysis has been performed for varying values of critical energy release rates, loading velocities and crack distributions. The crack orientation, length and positioning significantly alters the outcome of the temperature field.. A concept of dirty binder has been introduced in the system. The dependency of the modified binder with the damage and temperature field still needs to be quantified. This study can be extended by including the effect of crystal plasticity. Higher loading velocities can also be studied by introducing equation of state to the system.

## REFERENCES

## REFERENCES

- [1] J. Akhavan, *The chemistry of explosives*, 2nd ed., ser. RSC paperbacks. Cambridge, U.K.: Royal Society of Chemistry, 2004.
- [2] T. Liddiard, J. Forbes, and D. Price, “Physical evidence of different chemical reactions in explosives as a function of stress,” in *Ninth Symposium (International) on Detonation*, 1989, pp. 1235–1242.
- [3] J. Dick, “Effect of crystal orientation on shock initiation sensitivity of pentaerythritol tetranitrate explosive,” *Applied Physics Letters*, vol. 44, no. 9, pp. 859–861, 1984.
- [4] B. Asay, *Shock wave science and technology reference library, Vol. 5: Non-shock initiation of explosives*. Springer Science & Business Media, 2009, vol. 5.
- [5] M. Chaudhri and J. E. Field, “The role of rapidly compressed gas pockets in the initiation of condensed explosives,” *Proceedings of the Royal Society of London. A. Mathematical and Physical Sciences*, vol. 340, no. 1620, pp. 113–128, 1974.
- [6] J. Dienes, Q. Zuo, and J. Kershner, “Impact initiation of explosives and propellants via statistical crack mechanics,” *Journal of the Mechanics and Physics of Solids*, vol. 54, no. 6, pp. 1237–1275, 2006.
- [7] F. Zhou, J.-F. Molinari, and T. Shioya, “A rate-dependent cohesive model for simulating dynamic crack propagation in brittle materials,” *Engineering fracture mechanics*, vol. 72, no. 9, pp. 1383–1410, 2005.
- [8] G. A. Francfort and J.-J. Marigo, “Revisiting brittle fracture as an energy minimization problem,” *Journal of the Mechanics and Physics of Solids*, vol. 46, no. 8, pp. 1319–1342, 1998.
- [9] A. Griffith, “The theory of rupture,” in *First Int. Cong. Appl. Mech*, 1924, pp. 55–63.
- [10] J. L. Sanders, *On the Griffith-Irwin fracture theory*. Citeseer, 1959.
- [11] H. Ulmer, M. Hofacker, and C. Miehe, “Phase field modeling of brittle and ductile fracture,” *PAMM*, vol. 13, no. 1, pp. 533–536, 2013.
- [12] H. Amor, J.-J. Marigo, and C. Maurini, “Regularized formulation of the variational brittle fracture with unilateral contact: Numerical experiments,” *Journal of the Mechanics and Physics of Solids*, vol. 57, no. 8, pp. 1209–1229, 2009.
- [13] N. Grilli, C. A. Duarte, and M. Koslowski, “Dynamic fracture and hot-spot modeling in energetic composites,” *Journal of Applied Physics*, vol. 123, no. 6, p. 065101, 2018.

- [14] P. Chakraborty, Y. Zhang, and M. R. Tonks, “Multi-scale modeling of microstructure dependent intergranular brittle fracture using a quantitative phase-field based method,” *Computational Materials Science*, vol. 113, pp. 38–52, 2016.
- [15] C. A. Duarte, N. Grilli, and M. Koslowski, “Effect of initial damage variability on hot-spot nucleation in energetic materials,” *Journal of Applied Physics*, vol. 124, no. 2, p. 025104, 2018.
- [16] “Home.” [Online]. Available: <https://mooseframework.org/>
- [17] J. Bleyer, C. Roux-Langlois, and J.-F. Molinari, “Dynamic crack propagation with a variational phase-field model: limiting speed, crack branching and velocity-toughening mechanisms,” *International Journal of Fracture*, vol. 204, no. 1, pp. 79–100, 2017.
- [18] C. M. G. Amaro, “Dynamic fracture in brittle amorphous materials: Dissipation mechanisms and dynamically-induced microcracking in pmma,” Ph.D. dissertation, Ecole Polytechnique X, 2009.
- [19] I. Smirnov and Y. Sudenkov, “Crack propagation in pmma plates under various loading conditions,” in *ICF13*, 2013.
- [20] M. J. Borden, C. V. Verhoosel, M. A. Scott, T. J. Hughes, and C. M. Landis, “A phase-field description of dynamic brittle fracture,” *Computer Methods in Applied Mechanics and Engineering*, vol. 217, pp. 77–95, 2012.
- [21] T. Shioya, Y. Koga, K. Fujimoto, and R. Ishida, “Micro-mechanism of dynamic crack propagation in brittle materials,” *Le Journal de Physique Colloques*, vol. 49, no. C3, pp. C3–253, 1988.
- [22] P. D. Washabaugh and W. Knauss, “A reconciliation of dynamic crack velocity and rayleigh wave speed in isotropic brittle solids,” *International Journal of Fracture*, vol. 65, no. 2, pp. 97–114, 1994.
- [23] A. Dandekar, Z. A. Roberts, S. Paulson, W. Chen, S. F. Son, and M. Koslowski, “The effect of the particle surface and binder properties on the response of polymer bonded explosives at low impact velocities,” *Computational Materials Science*, vol. 166, pp. 170–178, 2019.
- [24] A. Barua, Y. Horie, and M. Zhou, “Microstructural level response of hmx–estane polymer-bonded explosive under effects of transient stress waves,” *Proceedings of the Royal Society A: Mathematical, Physical and Engineering Sciences*, vol. 468, no. 2147, pp. 3725–3744, 2012.
- [25] A. Barua and M. Zhou, “Heating in microstructures of hmx/estane pbx during dynamic deformation,” in *APS Shock Compression of Condensed Matter Meeting Abstracts*, 2011.
- [26] D. Williamson, C. Siviour, W. Proud, S. Palmer, R. Govier, K. Ellis, P. Blackwell, and C. Leppard, “Temperature–time response of a polymer bonded explosive in compression (edc37),” *Journal of Physics D: Applied Physics*, vol. 41, no. 8, p. 085404, 2008.
- [27] B. Banerjee and D. O. Adams, “Micromechanics-based prediction of thermoelastic properties of high energy materials,” *Constitutive Modeling of Geomaterials*, pp. 158–164, 2003.

- [28] Y. Long, Y. Liu, F. Nie, and J. Chen, "A method to calculate the thermal conductivity of hmx under high pressure," *Philosophical Magazine*, vol. 92, no. 8, pp. 1023–1045, 2012.
- [29] L. Koshigoe, R. Shoemaker, and E. Taylor, "Specific heat of hmx," *AIAA journal*, vol. 22, no. 11, pp. 1600–1601, 1984.
- [30] H. Kugler, R. Stacer, and C. Steimle, "Direct measurement of poisson's ratio in elastomers," *Rubber chemistry and technology*, vol. 63, no. 4, pp. 473–487, 1990.
- [31] F. R. Chaves and J. C. Góis, "Research on the specific heat capacity of pbx formulations based on rdx," *Journal of aerospace technology and management*, vol. 8, no. 3, pp. 352–356, 2016.
- [32] S. Palmer and J. Field, "The deformation and fracture of  $\beta$ -hmx," *Proceedings of the Royal Society of London. A. Mathematical and Physical Sciences*, vol. 383, no. 1785, pp. 399–407, 1982.
- [33] J. Lou, T. Zhou, Y. Zhang, and X. Zhang, "Numerical simulation study on thermal response of pbx 9501 to low velocity impact," in *AIP Conference Proceedings*, vol. 1793, no. 1. AIP Publishing, 2017, p. 030021.
- [34] R. A. Austin, N. R. Barton, J. E. Reaugh, and L. E. Fried, "Direct numerical simulation of shear localization and decomposition reactions in shock-loaded hmx crystal," *Journal of Applied Physics*, vol. 117, no. 18, p. 185902, 2015.
- [35] J. Mares, J. Miller, N. Sharp, D. Moore, D. Adams, L. Groven, J. Rhoads, and S. F. Son, "Thermal and mechanical response of pbx 9501 under contact excitation," *Journal of Applied Physics*, vol. 113, no. 8, p. 084904, 2013.
- [36] C. M. Tarver, S. K. Chidester, and A. L. Nichols, "Critical conditions for impact- and shock-induced hot spots in solid explosives," *The Journal of Physical Chemistry*, vol. 100, no. 14, pp. 5794–5799, 1996.
- [37] D. Idar, R. Lucht, J. Straight, R. Scammon, R. Browning, J. Middleditch, J. Dienes, C. Skidmore, and G. Buntain, "Low amplitude insult project: Pbx 9501 high explosive violent reaction experiments," Los Alamos National Lab., NM (United States), Tech. Rep., 1998.
- [38] L. Xue, O. Borodin, G. D. Smith, and J. Nairn, "Micromechanics simulations of the viscoelastic properties of highly filled composites by the material point method (mpm)," *Modelling and Simulation in Materials Science and Engineering*, vol. 14, no. 4, p. 703, 2006.
- [39] B. Banerjee and D. O. Adams, "On predicting the effective elastic properties of polymer bonded explosives using the recursive cell method," *International Journal of Solids and Structures*, vol. 41, no. 2, pp. 481–509, 2004.

## APPENDIX

## A. STEPS INVOLVED IN INITIALIZATION OF THE PHASE FIELD DAMAGE MODEL

This appendix describes the method involved in initializing and running simulations using the phase field damage model. The simulations are run in a software called MOOSE (Multi-physics object oriented simulation environment). The following files are needed to run the simulation in the cluster; a *.i* file that contains all the information including material parameters, boundary conditions, initial conditions, solver as well as the modules involving the implementation of the phase field damage model, a *.msh* file that contains information pertaining to mesh used in the system and an executable file that links all the libraries together. This input file is specific to MOOSE. At the end of the simulation a *.e* type output file is generated which is visualized using a open-source data analysis software called Paraview. The modules that contain information regarding the implementation of the phase field models are written in C++ and are linked to each other via the executable file. Finally a *.sub* file is used to submit the simulation to a cluster. These are the steps in chronological order involved in running a simulation:

- Mesh generation
  1. MOOSE has an inbuilt function that creates a mesh automatically. So for running regular symmetric meshes this feature is extremely useful.
  2. For meshes with specific details and features meshes have been prepared using Gmesh. Depending on the geometry either quad or triangular elements are used and a *.msh* file is generated to be used in MOOSE for the simulation.
- The input script.

1. An input scripts which contain information pertaining to Mesh scaling and initialization,initial conditions, loading characteristics, boundary conditions, kernels and modules being used for the Phase field model,material properties and solvers is prepared.
  2. This *.i* type file is submitted to the cluster along with the executable file.
- Submission file
    1. A submission file is prepared which contains data pertaining to the selection of cluster, number of nodes and time needed to run the simulation.
    2. The simulation is run using the cluster file and finally an output file is obtained.
  - Data visualization
    1. A *.e* type output file is obtained which is visualized by using Paraview.